14

15

16

Tropical forcing of Australian extreme low minimum 1 temperatures in September 2019 2 3 Eun-Pa Lim¹, Harry H. Hendon¹, Li Shi¹, Catherine de Burgh-Day¹, Debra Hudson¹, Andrew 4 King², Blair Trewin¹, Morwenna Griffiths¹ and Andrew Marshall¹ 5 6 ¹ Bureau of Meteorology, Melbourne, VIC, Australia 7 8 ² School of Earth Sciences and ARC Centre of Excellence for Climate Extremes, University 9 of Melbourne, Parkville, VIC, Australia 10 Corresponding author: 11 harry.hendon@bom.gov.au ORCID ID: https://orcid.org/0000-0002-4378-2263 12 13

To be submitted to Climate Dynamics

13 July 2020

20

Abstract

17

We explore the causes and predictability of extreme low minimum temperatures (Tmin) that 18 occurred across northern and eastern Australia in September 2019. Historically, reduced 19 Tmin is related to the occurrence of a positive Indian Ocean Dipole (IOD) and central Pacific 20 El Nino. Positive IOD events tend to locate an anomalous anticylone over the Great 21 Australian Bight, therefore inducing cold advection across eastern Australia. Positive IOD 22 and central Pacific El Nino also reduce cloud cover over northern and eastern Australia, thus 23 24 enhancing radiative cooling at night-time. During September 2019, the IOD and central Pacific El Nino were strongly positive, and so the observed Tmin anomalies are well 25 26 reconstructed based on their historical relationships with the IOD and central Pacific El Nino. 27 This implies that September 2019 Tmin anomalies should have been predictable at least 1-2 months in advance. However, even at zero lead time the Bureau of Metereorolgy ACCESS-28 S1 seasonal prediction model failed to predict the anomalous anticyclone in the Bight and 29 the cold anomalies in the east. Rather, the model predicted a circulation amomaly reminiscent 30 of the low phase of the Southern Annular Mode (SAM). Analysis of hindcasts for 1990-2012 31 indicates that the model's teleconnections from the IOD are systematically weaker than the 32 observed, which likely stems from mean state biases in sea surface temperature and rainfall in 33 the tropical Indian and western Pacific Oceans. This weak teleconnection possibly allowed 34 35 for the incorrect early expression of negative SAM following the strong polar stratospheric warming that occurred in late August 2019. 36

37

38

Key words: Extremes; Predictability; Teleconnections;

1. Introduction

Climate anomalies during 2019 were extraordinary across the globe with the concurrence of a central Pacific El Nino¹ (also referred to as El Nino Modoki or warm-pool El Nino) event (Ashok et al. 2007; Kao and Yu 2009; Kug et al. 2009), a near-record strength positive Indian Ocean Dipole mode event (IOD; Saji et al. 1999), and a record-strong weakening and warming of the Southern Hemisphere stratospheric polar vortex and subsequent development of record-strong negative phase of the Southern Annular Mode event (SAM; Thompson and Wallace 2000) during September-December (Lim et al. 2020a). All these phenomena are well-known to drive hot and dry conditions over Australia especially during austral spring and summer (Saji et al. 2005; Hendon et al. 2007; Wang and Hendon 2007; Ummenhofer et al. 2009; Risbey et al. 2009; Marshall et al. 2014; Lim and Hendon 2015; Lim et al. 2019). Indeed, Australian areal-mean monthly mean maximum temperature was in the top decile category and monthly mean rainfall was in the bottom decile category during September to December 2019 based on 110- and 120-year observational records, respectively². Austral spring (September to November) and the individual months of November and December 2019 were also the driest on record.

In stark contrast to the significantly higher-than-normal monthly mean (hereafter, referred to as monthly) maximum temperatures, monthly minimum temperatures were significantly lower than normal in many locations over Australia during August and September in 2019 (Fig 1). Anomalously low minimum temperatures can have a significant impact on a wide range of agricultural industries: For instance, damage to crops due to one or more severe frosts is a major risk for agriculture in Australia (Frederiks et al. 2015; Zheng et al. 2015), and productivity of beef and dairy cattle (Webster et al. 2008; Cowan et al. 2019),

¹ The term "central Pacific El Nino" is used in this study to describe an event whose maximum SST anomaly is found near the dateline. This will not necessarily correspond to an event in the eastern Pacific.

² http://www.bom.gov.au/climate/change/#tabs=Tracker&tracker=timeseries

cotton (Bange and Milroy 2004), rice (Jacobs and Pearson 1999; Hatfield and Prueger 2015), sugarcane (Grantz 1989), and viticulture (Keller et al. 2010) is also sensitive to significantly lower than normal temperatures. Despite such substantial impacts of low minimum temperatures on the productivity of primary industry, relatively little attention has been paid to understanding the causes and predictability of low minimum temperatures over Australia as compared to maximum temperatures and rainfall, although there has been a growing volume of research regarding frosts (Dittus et al. 2014; Crimp et al. 2016a; Grose et al. 2018; Risbey et al. 2019). Therefore, we have attempted to improve our understanding of the variability and predictability of low minimum temperatures over Australia by examining the cold extreme case of September 2019. Because cold extremes potentially have a significant impact on agriculture in spring by influencing the plant life cycle, including the timing of the flowering of winter crops (Crimp et al. 2016a), we have focused on the anomalously low minimum temperature (Tmin) of September 2019, for which many regions of northern and eastern Australia experienced September-mean Tmin in the bottom two deciles, although south-eastern Australia also experienced extreme low minimum temperatures in August 2019 (Fig 1).

62

63

64

65

66

67

68

69

70

71

72

73

74

75

76

77

78

79

80

81

82

83

84

85

In this study, we first investigate what caused the widespread low minimum temperatures during September 2019, which is especially intriguing given the enormous interest in the hot and dry conditions that occurred later in austral spring 2019 across eastern Australia and the subsequent spate of devastating bushfires

(http://www.bom.gov.au/climate/current/statements/scs72.pdf) (Boer et al. 2020). We also assess the predictability of the occurrence of extreme low minimum temperatures during September 2019 using the Australian Bureau of Meteorology (BoM)'s dynamical sub-seasonal to seasonal climate forecast system ACCESS-S1 (the Australian Community Climate and Earth

System Simulator-Seasonal prediction system version 1; Hudson et al. 2017) with an aim to elucidate areas for improvement in the future development of the forecast system.

2. Data and Forecast System

86

87

88

89

90

91

92

93

94

95

96

97

98

99

100

101

102

103

104

105

106

107

108

109

For the observational analysis of Australian temperatures and rainfall, we used the Australian Water Availability Project (AWAP) monthly mean gridded analyses of daily maximum temperature (Tmax), daily minimum temperature (Tmin) and rainfall, which are provided on a 5 km grid (Jones et al. 2009). Tmax and Tmin are indicative of the 2 m air temperature as measured, for instance, in a meteorological screen. Three extreme indices (adapted from Zhang et al. 2011) were also calculated at each grid point using the daily AWAP Tmin analyses: the coldest minimum temperature of the month, and the number of days with daily minimum temperatures below 2°C and 0°C. Frost occurs when the ground temperature drops to freezing (or below). Frost can occur when the 2 m air temperarture is as warm as 2°C as a result of a near surface inversion due to enhanced surface radiative cooling (Kalma et al.1992). A hard frost (or freeze) is assumed to have occurred when the 2 m temperature drops to 0° C (or below). We investigate atmospheric circulation anomalies using the analyses of mean sea level pressure (MSLP), 10-m zonal (U) and meridional (V) winds and total cloud cover fraction from the Japanese 55-year ReAnalysis (JRA-55), which are provided daily on a ~55 km horizontal grid (Kobayashi et al. 2015). For sea surface temperature (SST), we use the Hurrell et al. (2008) monthly mean analyses, which is based on the HadISST analyses (Rayner et al. 2003) up through 1981 that is mergerd with the Reynolds et al. (2002) optimum interpolation version 2 SST analyses for 1982-2019.

Anomalies of all the observational variables were computed relative to the climatological mean over 1990-2012, which is the period when the ACCESS-S1 hindcasts are available. Trends were removed from all the observational data in order to focus on the

interannual variability of Tmin. The AWAP Tmin analysis shows few areas of strong trends in September during the period 1979-2018 except in the far south of Queensland, where there is a warming trend, and in some locations of Western Australia, where there is a cooling trend³ (statistically significant at the 10% level, assessed by a two-tailed Student's t-test; Supplementary Fig S1). Correlation and regression analyses using the observational data were conducted for 1979-2018.

Forecasts of Australian Tmin and associated large-scale circulations were produced from ACCESS-S1 (Hudson et al. 2017). This system, which is based on the UKMO GloSea5 system (MacLachlan et al. 2015), is a state-of-the-art dynamical sub-seasonal to seasonal climate forecast system, which became operational at BoM in August 2018. The atmosphere is resolved on a ~60 km grid with 85 vertical levels, fully resolving the stratosphere. The ocean is resolved at 25 km with 75 vertical levels. The atmosphere, land and ocean component models are coupled every three hours.

11-member hindcasts of ACCESS-S1 out to 6-month lead time are available for 1990-2012 at four different initialisation dates per month (1st, 9th, 17th and 25th). The model atmosphere (zonal and meridional winds, temperatures, humidity and surface pressure) and soil temperatures were initialised using the European Centre for Medium-Range Forecasts Interim Reanalysis (ERA-Interim) data (Dee et al. 2011), while the model soil moisture was initialised with the climatology of ERA-Interim (over 1990-2012) (MacLachlan et al. 2015). The ocean was initialised with the analysis from the Met Office Forecast Ocean Assimilation Model (FOAM; Waters et al. 2015).

The 11-member ensemble was produced by perturbing the atmospheric initial conditions only (Hudson et. al. 2017). For this study, we have formed a 22 member ensemble

³ This is potentially influenced by a cool bias in recent AWAP Tmin data, relative to the homogenised ACORN-SAT dataset, driven in part by the movement of sites from town to out-of-town locations in the 1990s and 2000s (Trewin2018, Trewin et al. 2020).

by utilising the forecasts initialised on the 1st of a month and the 25th of the previous month. For instance, the lead time 0 forecasts for September consists of the 11-member ensemble forecasts initialised on the 1st of September and the 11-member ensemble forecasts initialised on the 25th of August.

The real-time forecasts using the operational system for September 2019 were initialised with the atmospheric conditions from BoM's numerical weather prediction system (similar atmospheric model to ACCESS-S1 but with higher horizontal resolution) and the ocean conditions provided from FOAM. The real-time system produces an 11-member ensemble of forecasts everyday. Generation of forecast products provided by the BoM Climate Service uses a lagged ensemble approach to form a 99-member ensemble (9 consecutive days for the seasonal forecast products). For this study, we formed a 22-member ensemble by combining the eleven members from the real-time forecasts initialised on the 1st of a month and on the 25th of the previous month to be consistent with our hindcast analysis. Further details of the ACCESS-S1 model configuration, initialisation, ensemble generation and forecast performance can be found in Hudson et al. (2017).

3. Results

3.1 Cold extremes in September 2019

The monthly Tmin for September 2019 was anomalously low over northern and eastern Australia, which contrasted to the higher than normal Tmin over the southern half of Western Australia (Fig 2). Some parts of northern and eastern Australia experienced Tmin in the bottom 20% (i.e., bottom quintile) based on 110-year data (Fig. 1b). If we consider the most recent 40 years, Tmin anomalies in September 2019 are in the extreme cold categories (bottom 20%) over larger areas in the north and the east, in stark contrast to the Tmin anomalies in southern Western Australia, which are in the top 10% (i.e., top decile) (Supplementary Fig S2).

The lowest minimum temperatures in September 2019 were up to 4°C lower than normal over the northern parts of Northern Territory and Western Australia and the northeast of Queensland (Fig 2b). Moreover, the southernmost part of the Australian continent, especially over eastern South Australia, northern Victoria and parts of southern inland New South Wales, experienced an above-average number of days with Tmin below 2 °C, a common threshold for potential frost formation (e.g., Kalma et al. 1999), and some areas even had an above-average number of days of hard frost with Tmin below 0 °C (Figs 2c,d). The increased number of days with Tmin below 0 °C is concentrated over the Great Dividing Range in the south east of the continent and reflects an orographic lowering of Tmin values. The pattern of enhanced occurrence of days with September Tmin < 0 °C and 2 °C in the south east of the country is typical of what occurs during this month when the local monthly Tmin is below normal (Fig. 3)⁴.

3.2 Drivers of cold nights over northern and eastern Australia

To investigate what drives the interannual variability of September minimum temperature of Australia, with the ultimate goal to understand what caused the 2019 September Tmin anomaly, we first explore the link to tropical SST variations. We do this by regressing detrended gridded SST on the inversely signed eastern Australian areal-mean Tmin (averaged over land points east of 140°E and north of 45°S) for September using data for 1979-2018 (Fig 4b) (the inverse Tmin was used to highlight the SST pattern associated with lower-than-normal minimum temperatures). The regression pattern bears a signature of the positive

⁴ Here we have used the Spearman rank correlation to relate the occurrences of days with Tmin < 0 and 2 °C to the monthly Tmin at each gridpoint because the relationship may not be linear although we assume the relationship between monthly Tmin and number of days below a threshold is monotonic (i.e., number of days below 0 and 2°C increases with lower values of monthly mean Tmin).

phase of the Indian Ocean Dipole (IOD), which is characterised by colder than normal sea surface in the tropical eastern Indian Ocean (0-10°S,90-110°E) and concurrent warmer than normal sea surface in the tropical western Indian Ocean (10°S-10°N,50-70°E; Saji et al. 1999). Although eastern Australia Tmin is more correlated with the SST in the eastern pole of the IOD, during September the SST in the eastern pole of the IOD is correlated with the index of the IOD, the Dipole Mode Index (DMI), at 0.9. Thus, we can subsequently quantify the relationship of Tmin with the tropical Indian Ocean SST variations using the DMI.

Eastern Australian Tmin is also seen to be significantly related to the occurrence of central Pacific (CP) El Nino, which is characterised by warmer than normal sea surface in the vicinity of the equatorial dateline (10°S-10°N, 165-220°E) flanked by colder than normal SSTs in the far east (15°S-5°N, 250-290°E) and west (10°S-20°N, 125-145°E; Ashok et al. 2007).

The observed SST anomaly in September 2019 (Fig. 4a) shows a pattern of both positive IOD and CP El Nino, which is quantified by positive amplitudes greater than one standard deviation (σ) of the DMI from May 2019 until January 2020; and the El Nino Modoki Index (EMI; Ashok et al. 2007) from April to October 2019 (Supplementary Fig.S3). In September 2019, the DMI was +1.6σ, which was the 2nd highest after 1994, and the EMI was +1.2σ, the 3rd highest after 2004 and 1994 for the month in the past 40 year records (Fig 4c). Eastern Australian Tmin (EAU Tmin) for September 2019 was the 4th coldest in the same period. The lowest mean minimum temperature over eastern Australia for September occurred in 1994, with slightly larger DMI and EMI values than 2019 (Fig. 4c).

Over 1979-2018, the correlation of EAU Tmin with the DMI and with EMI is -0.4 and -0.6, respectively. Spatially, the significant correlation of monthly Tmin during September with the DMI is concentrated in the southeast along the Dividing Range and in the far northwest (Fig. 5a), whereas the significant correlation with the EMI is mainly in the

central north and east (Fig. 5b). The high correlation of the DMI with the number of days with Tmin < 0 and 2 °C is similarly localised in the southeast along the Dividing Range (Figs. 5c,e), whereas the high correlation with the EMI is concentrated in the eastern Murray-Darling Basin(Figs. 5d.f). Similar correlation patterns of the monthly Tmin are found between the lowest Tmin and the DMI and the EMI (Figs. 5g,h).

Based on these relationships in Figure 5, we can reconstruct Tmin anomalies with multiple linear regression using the DMI and the EMI as predictors. The explained variance of monthly Tmin for September using this regression model is displayed in Fig. 6a (expressed as the correlation of reconstructed Tmin with observed Tmin over the period 1979-2018). The explained variance ranges up to 60% along the east coast and extending across the far north. This regression model then can be used to successfully reconstruct the September 2019 observed anomalies (Fig. 6b) by plugging in the observed values of the DMI and EMI for September 2019 (Fig. 6c). The correlation between the observed and the reconstructed Tmin anomaly patterns for 2019 (i.e., pattern correlation between Fig 6b and 6c) is 0.8.

In order to gain more insight into the cause of the widespread low Tmin for September 2019, we display in the top row of Figure 7 the anomalies of MSLP, 10-m horizontal winds and total cloud cover fraction for September 2019. To assist comparison with the lower panels, we display the observed September 2019 Tmin anomaly map (Fig. 2a) here again (Figure 7e). The middle and bottom rows of Figure 7 display the composite anomalies during the five strongest positive IOD events and the three strongest CP El Nino events observed during 1979-2018 (years are listed in Table 1), respectively. The observed 2019 circulation anomalies are characterised by a strong high pressure anomaly centered over the Great Australian Bight and associated significant northward winds advecting cold air from the south and westward winds blowing towards Western Australia. Also, there is a 4-16% reduction in the total cloud cover fraction over northern and eastern Australia, which

would have increased outgoing longwave radiation (i.e. radiative cooling to space), therefore promoting enhanced night-time cooling. These circulation and cloud fraction anomalies are remarkably similar to what typically occurs during positive IOD years (middle row of Fig. 7) and, to a lesser degree, during the strong CP El Nino years (bottom row Fig. 7). The analysis presented in Figure 7 confirms the important role of the IOD and central Pacific El Nino for promoting the low Tmin anomalies observed during September 2019.

We have also examined the composite anomalies for strong negative IOD years and strong CP La Nina years and found that the circulation anomalies are not symmetrically opposite to their positive counterparts over the midlatitudes (Supplementary Fig. S4), and the pressure anomalies and related horizontal wind anomalies are mostly not statistically significant at the 10% level. On the other hand, negative IOD and CP La Nina are related to significant low pressure anomalies in the tropical eastern Indian Ocean and over the Maritime Continent and significant increases of total cloud cover over eastern Australia (Supplementary Fig S4). These anomalous conditions appear to be closely tied to higher Tmin over the north and the subtropical east of the country observed during the negative IOD and CP La Nina years.

3.3 ACCESS-S1 Forecasts

IOD events generally start to develop during austral winter, peak in late spring and then typically decay in December when the Australian summer monsoon commences (Saji et al. 1999b; Zhao and Hendon 2009; Hendon et al. 2012). The skill for predicting the IOD, as expressed by temporal correlation of the predicted and observed DMI, based on ACCESS-S1 hindcasts from 1990-2012, is displayed in Figure 8a. There is little skill in predicting the IOD for start dates prior to June, and the highest skill at long lead times is for the August to October start dates. The forecast performance of ACCESS-S1 for the IOD is similar to other coupled model seasonal prediction systems (Zhao and Hendon 2009; Shi et al. 2012).

However, even from September and October start dates, the forecast skill drops off for austral summer months because the IOD rapidly decays in December. Consistent with the lack of hindcast skill to predict the IOD prior to June or July start times, the predicted DMI index for September 2019 did not display realistically large amplitude until forecasts initialized on 1 July (Fig. 8c).

In contrast to the IOD, CP El Nino/La Nina can be skilfully predicted by ACCESS-S1, based on correlation of predicted and observed EMI, for start times all year round (Fig, 8b). The long lead skill reflects the long persistence of the EMI (Hendon et al. 2009; Kug et al. 2009; Fig 8b). However, the highest long lead skill for the EMI is for start times after May, which is after the so-called "northern spring predictability barrier". Although positive EMI anomalies are consistently predicted from as early as 1 April 2019, the predicted anomalies are consistently weaker than observed (Fig. 8c).

In light of the strong capability to predict both IOD and CP El Nino at least for short lead times in the late winter and spring, we further assess the capability of ACCESS-S1 to predict Tmin extremes across Australia by computing the Receiver Operating Characteric (ROC; also called the relative operating characteristic; Wilks 2006) curve using the hindcasts for 1990-2012 over all grid points of Australia (Figs. 9a,9b) and the area under the ROC curve at each grid point (Figs. 9c,9d) at zero (forecasts initialised on 1 September) and one month (forecasts initialised on 1 August) lead times. The ROC is computed as the ratio of the hit rate⁵ versus false alarm rate⁶ for predicting Tmin in the lowest quintile. The ROC is computed in ten equally sized probability thresholds from 0 to 1. In Figures 9a, 9b, the curve above the no skill line indicates good forecast performance as it indicates greater hit rates than false alarm rates no matter what are the probability thresholds to issue an alarm for an

⁵ The ratio of the correct forecasts for the occurrence of an event to the total number of forecasts

⁶ The ratio of the incorrect forecasts for the occurrence of an event (i.e., forecasts for the occurrence which are not observed) to the total number of forecasts

event occurrence. For the area under the ROC curve, values greater than 0.5 are skilful relative to a random forecast and a value of 1 is perfect.

ACCESS-S1 shows overall high skill to predict low Tmin for September at both lead times, and the significantly high skill across much of eastern and northern Australia at zero lead time (Fig. 9a) is where the observed low values of Tmin occurred during 2019 (Fig. 2a). Although the skill declines at lead time of 1 month (Fig. 9b), skill remains high in the central east and north, suggesting that the anomalies during 2019 might have been well predicted. However, the forecast for September 2019 (Figs. 10a and b) failed to capture the extreme low Tmin across the east at lead time 0 and across the east and the north at lead time 1 month. These forecast busts imply a missed opportunity to forewarn the increased chance of the lower-than-normal minimum temperatures and frost formation in southern New South Wales, Victoria and eastern South Australia during September 2019. This forecast error appears to be related to the complete miss of the teleconnection of the positive IOD to locate a high pressure anomaly over the Bight (Figs. 10 c,d) that drives northward and westward winds advecting the cold air over eastern Australia. Why did these forecast errors happen?

The capability of ACCESS-S1 to capture telecponnections from the IOD and CP El Nino is assessed by examining composite patterns of MSLP, 10-m horizontal winds, outgoing longwave radiation flux (used as a proxy for total cloud cover) and Tmin during September for the strong positive IOD years and strong positive CP El Nino (not including 2019) using forecast data at zero lead time (Fig. 11). For the IOD, the predicted patterns have an overall resemblance to the observed composite patterns shown in Figure 7 (middle row and also Supplementary Fig S5 for the same composite years), but the magnitudes of the anomalies are significantly smaller than the observed even at this shortest lead time. The surface pressure anomaly is especially too weak and too far south compared to the observed. The composite patterns for MSLP and horizontal winds for CP El Nino (Figs. 11f-h) show the

inability of ACCESS-S1 to simulate the high pressure center southwest of Australia and associated circulation. The composite forecast anomalies are also not significantly different from the normal conditions, highlighting that the teleconnections of the positive IOD and CP El Nino to Australian Tmin are substantially underpredicted in ACCESS-S1. Consequently, lower than normal Tmin in September during positive IOD and CP El Nino appear to be correctly predicted only in the far north of the country but are not captured in the south and east where the effects of the high pressure anomaly in the Bight are important (Figs. 11e,j).

The inability of ACCESS-S1 to capture the impact of the positive IOD and CP El Nino on Tmin throughout a broad region of central and southern Australia is likely related to the systematic errors in simulation of the mean state of the tropical Indo-Pacific: the SST tends to be simulated to be too cold to the north west of Australia, with too little rainfall, and stronger than observed south easterly trade winds across the southern tropical Indian Ocean (Hudson et al. 2017). As the tropical Indian Ocean and western Pacific are where SST is high and associated convective rainfall is rich, the cold and dry mean state biases are translated into problems in simulating the teleconnection from the IOD to the extratropics (Hudson et al. 2017).

However, examination of the forecast for September 2019 (Figs. 10e,f) suggests that the model error of this particular case well exceeds the systematic errors in the depiction of the IOD and CP El Nino teleconnection that were discussed above. Closer inspection of the forecast surface pressure anomaly (Figs. 10e,f) reveals that the model was predicting strong low pressure anomalies south of Australia, which were a midlatitude signature of a strong negative phase of the SAM (predicted September SAM at lead zero -0.7σ but observed SAM was +0.6σ; Lim et al. 2020b). Strong negative SAM was predicted for September 2019 as a result of the record-strong Antarctic polar stratospheric warming that occurred in the last week of August 2019 (Lim et al. 2020b; Rao et al. 2020). Consequently, clearer sky and

increased downward compression of air over the Australian continent, which are known as the responses to the negative SAM (Lim et al. 2019), were predicted (Figs. 10c,d,g,h), resulting in high Tmin being adiabatically promoted in the model. However, in reality, the stratospheric warming did not couple down to the surface until the 3rd week of October, and so the SAM was actually positive in September (Lim et al. 2020b); and a pronounced high pressure anomaly associated with the positive IOD was dominant over the Bight as shown in Figure 7a. We can speculate that ACCESS-S1 was prematurely predicting negative SAM during September in response to the stratospheric warming because of the too-weak teleconnection from the IOD and CP El Nino. Rao et al. (2020) demonstrated that the same error of predicting negative September SAM in 2019 was found in the multi-model mean prediction consisting of the five different major international centre models. Thus, further work is required to better understand the source of this common error across the forecast systems.

To further gain insight into the apparently high skill for predicting Tmin across much of the east but the failure during 2019, we also assess the capability of ACCESS-S1 to depict the Tmin anomalies associated with the negative IOD and CP La Nina (compare Supplementary Fig S7 to Figs S4 and S6). For these cases, the model does a much better job in capturing the higher-than-normal Tmin over the north and subtropical east of Australia as observed. Therefore, the forecast skill for September Tmin across much of the east and north as shown in Figure 9, seems to reflect the forecast skill in predicting Tmin during negative IODs and CP La Ninas.

4. Concluding remarks

Northern and eastern Australia experienced very unusual low minimum temperatures during September 2019, which were recorded to be in the bottom two deciles based on the past 40 year record. The number of days with minimum temperatues below 2°C and 0°C, which are indicators of potential frost damage, was significantly larger along and north of the Dividing Range in Victoria, South Australia and southern New South Wales, indicating a potential increase of frost formation. We have shown that, historically, reduced September-mean Tmin across northern and eastern Australia is related to the occurrence of the positive IOD and CP El Nino, which are monitored by the DMI and the EMI, respectively. The teleconnection of the positive IOD to the Southern Hemisphere extratropics is characterised by a well-defined high pressure anomaly over the Great Australian Bight (e.g. Cai et al. 2011; McIntosh and Hendon 2017), which promotes cold air advection from the south to eastern Australia. Furthermore, for both positive IOD and CP El Nino, reduced cloud cover in the northern and eastern portions of Australia is associated with lower Tmin, allowing more outgoing longwave radiation at night.

In September 2019 the IOD was the 2nd strongest positive and central Pacific El Nino was the 3rd strongest for the month in the past 40-year record. The observed 2019 September Tmin anomalies are well reconstructed using regressions onto the DMI and EMI during the period 1979-2018, then scaling the coefficients by the amplitude of the DMI and EMI in September 2019. This reconstruction suggests that the September 2019 Tmin anomalies should be well predicted because September IOD is skilfully predictable at least with 2 month lead time and September central Pacific El Nino is skilfully predictable at beyond 2 seasons lead time using the ACCESS-S1 system. However, even at zero lead time, ACCESS-S1 failed to predict the cold conditions over eastern Australia of September 2019 largely because of its failure to predict the anomalous high in the Bight that is predominantly associated with the positive IOD and, to a lesser extent, with central Pacific El Nino.

Analysis of the ACCESS-S1 hindcasts indicates that the simulated IOD and central Pacific El Nino teleconnections are systematically too weak to drive the Tmin variability in

eastern Australia and especially in the south, which leads to forecast busts at a time when cold extreme forecasts can be very important and useful over south eastern Australia. This weak teleconnection may have allowed for the incorrect early expression of negative SAM following the sudden stratospheric warming that occurred in late August 2019. The cause of the too weak IOD teleconnection is the focus of ongoing work, but presumably reflects in part the strong systematic biases in the mean state of the tropical Indian Ocean (e.g. Hudson et al. 2017) that are key to faithful depiction of the IOD.

The extreme Tmin that occurred in September 2019 also coincided with both drought and extreme high day-time temperatures over much of south-eastern and eastern Australia, driven by the strongly positive IOD and central Pacific El Nino. This is a critical time of year for many agricultural sectors in Australia that are sensitive to any one of these local climate extremes, and so exposure to all three simultaneously places significant stress on the industry. Therefore, understanding the drivers of these conditions and the pathways to improved prediction skill of Tmin in association with IOD and EMI should be a high priority of research.

Acknowledgement

This project is supported by funding from the Australian Government Department of Agriculture and Water Resources as part of its Rural R&D for Profit programme. Andrew King was supported by the Australian Research Council (DE180100638). We thank Dr Peter Hayman at SARDI for the useful discussion on the subject of this study and Drs Sharmila Sur and Guomin Wang at the BoM for their constructive feedback on the manuscript. This research was undertaken on the NCI National Facility in Canberra, Australia, which is supported by the Australian Commonwealth Government. The NCAR Command Language (NCL; http://www.ncl.ucar.edu) version 6.4.0 and IDL version 8.7.3 were used for data

399	analysis and visualization of the results. We also acknowledge NCAR/UCAR and JMA for
400	producing and providing the Hurrell et al. (2008) SST analysis and the JRA-55 reanalyses.
401	Disclosures
402 403 404	Funding : Support was provided from the Australian Government Department of Agriculture and Water Resources as part of its Rural R&D for Profit programme. Andrew King was supported by the Australian Research Council (DE180100638).
405 406	Conflicts of interest/Competing interests: The authors declare that they have no conflict of interest.
407	Availability of data and material:
408	The JRA-55 reanalyses are available from http://search.diasjp.net/en/dataset/JRA55
409 410 411	The Hurrell SST analyses are available from: https://climatedataguide.ucar.edu/climate-data/merged-hadley-noaaoi-sea-surface-temperature-sea-ice-concentration-hurrell-et-al-2008.
412 413 414 415	The AWAP Australian temperature and rainfall analyses are available from the Australian Bureau of Meteorology: "Australian Gridded Climate Data (AGCD) / AWAP; v1.0.0 Snapshot (1900-01-01 to 2018-12-31)". Downloaded from https://doi.org/10.4227/166/5a8647d1c23e0.
416 417	The ACCESS-S1 hindcasts and real time prediction system are described in Hudosn et al. (2017).
418 419 420	Code availability : The NCAR Command Language (NCL; http://www.ncl.ucar.edu) version 6.4.0 and IDL version 8.7.3 were used for data analysis and visualization of the results.

References

423

Ashok K, Behera SK, Rao SA, et al (2007) El Niño Modoki and its possible teleconnection. J 424 Geophys Res Ocean 112:. https://doi.org/10.1029/2006JC003798 425 Bange MP, Milroy SP (2004) Impact of short-term exposure to cold night temperatures on 426 427 early development of cotton (Gossypium hirsutum L.). Aust J Agric Res 55:655–664 Cai W, van Rensch P, Cowan T, Hendon HH (2011) Teleconnection pathways of ENSO and 428 the IOD and the mechanisms for impacts on Australian rainfall. J Clim 24:3910–3923. 429 https://doi.org/10.1175/2011JCLI4129.1 430 Cowan T, Wheeler MC, Alves O, et al (2019) Forecasting the extreme rainfall, low 431 432 temperatures, and strong winds associated with the northern Queensland floods of February 2019. Weather Clim Extrem 26:100232 433 434 Crimp SJ, Gobbett D, Kokic P, et al (2016a) Recent seasonal and long-term changes in southern Australian frost occurrence. Clim Change 115-128. 435 436 https://doi.org/10.1007/s10584-016-1763-5 Crimp SJ, Gobbett D, Kokic P, et al (2016b) Recent seasonal and long-term changes in 437 southern Australian frost occurrence. Clim Change 115–128. 438 439 https://doi.org/10.1007/s10584-016-1763-5 Dee D, Uppala S, Simmons a., et al (2011) The ERA - Interim reanalysis: Configuration and 440 performance of the data assimilation system. Quaterly J R Meteorol Soc 137:553–597. 441 https://doi.org/10.1002/qj.828 442 Dittus, A.J., Karoly, D.J., Lewis, S.C. and Alexander, L.V. (2014) An investigation of some 443 unexpected frost day increases in southern Australia. Aust Meteorol Ocean J, 64, 444 445 pp.261-271.

446	Frederiks TM, Christopher JT, Sutherland MW, Borrell AK (2015) Post-head-emergence	
447	frost in wheat and barley: defining the problem, assessing the damage, and identifying	
448	resistance. 66:3487–3498. https://doi.org/10.1093/jxb/erv088	
449	Grantz DA (1989) Effect of cool temperatures on photosynthesis and stomatal conductance in	
450	field-grown sugarcane in Hawaii.No Title. F Crop Res 22:143-155	
451	Grose MR, Black M, Risbey JS, et al (2018) Severe Frosts in Western Australia in September	
452	2016. 2014–2018. https://doi.org/10.1175/BAMS-D-17-0088.1	
453	Hatfield JL, Prueger JH (2015) Temperature extremes: Effect on plant growth and	
454	development. Weather Clim Extrem 10:4–10.	
455	https://doi.org/10.1016/j.wace.2015.08.001	
456	Hendon HH, Lim E-P, Liu G (2012) The Role of Air-Sea Interaction for Prediction of	
457	Australian Summer Monsoon Rainfall. J Clim 25:1278–1290.	
458	https://doi.org/10.1175/JCLI-D-11-00125.1	
459	Hendon HH, Lim E, Wang G, et al (2009) Prospects for predicting two flavors of El Niño.	
460	Geophys Res Lett. https://doi.org/10.1029/2009GL040100	
461	Hendon HH, Thompson DWJ, Wheeler MC (2007) Australian Rainfall and Surface	
462	Temperature Variations Associated with the Southern Hemisphere Annular Mode. J	
463	Clim 20:2452–2467. https://doi.org/10.1175/JCLI4134.1	
464	Hudson et. al. D (2017) ACCESS-S1 The new Bureau of Meteorology multi-week to	
465	seasonal prediction system. J South Hemisph Earth Syst Sci 67:132–159.	
466	https://doi.org/10.22499/3.6703.001	
467	Hurrell JW, Hack JJ, Shea D, et al (2008) A new sea surface temperature and sea ice	
468	boundary dataset for the community atmosphere model. J Clim 21:5145-5153.	

169	https://doi.org/10.11/5/2008JCL12292.1	
170	Jacobs BC, Pearson CJ (1999) Growth, Development and Yield of Rice in Response to Cold	
171	Temperature. J Agron Crop Sci 182:79–88	
172	Jones D, Wang W, Fawcett R (2009) High-quality spatial climate data-sets for Australia.	
173	Aust Meteorol Oceanogr J 58:233–248. https://doi.org/10.22499/2.5804.003	
174	Kalma J.D., Laughlin G.P., Caprio J.M., Hamer P.J.C. (1992) The Occurrence of Frost:	
175	Types, Distribution and Prediction. In: The Bioclimatology of Frost. Advances in	
176	Bioclimatology, vol 2. Springer, Berlin, Heidelberg.	
177	Keller M, Tarara JM, Mills LJ (2010) Spring temperatures alter reproductive development in	
178	grapevines. Aust J Grape Wine Res 16:445–454	
179	Kobayashi S, Ota Y, Harada Y, et al (2015) The JRA-55 Reanalysis: General specifications	
180	and basic characteristics. J Meteorol Soc Japan Ser II 93:5-48.	
181	https://doi.org/10.2151/jmsj.2015-001	
182	Kug J-S, Jin F-F, An S-I (2009) Two Types of El Niño Events : Cold Tongue El Niño and	
183	Warm Pool El Niño. J Clim 22:1499–1515. https://doi.org/10.1175/2008JCLI2624.1	
184	Lim E, Hendon HH, Butler AH, et al (2020a) The 2019 Antarctic sudden stratospheric	
185	warming. SPARC Newsl. 54 10–13	
186	Lim E, Hendon HH, Butler AH, et al (2020b) The Southern Hemipshere polar stratospheric	
187	warming and its impacts. Submitted to Bull. Amer. Met. Soc.	
188	Lim E, Hendon HH, Boschat G, et al (2019) Australian hot and dry extremes induced by	
189	weakenings of the stratospheric polar vortex. Nat Geosci.	
190	https://doi.org/10.1038/s41561-019-0456-x	

491 Lim E, Hendon HH (2015) Understanding the contrast of Australian springtime rainfall of 1997 and 2002 in the frame of two flavors of El Niño. J Clim 28:2804-2822. 492 https://doi.org/10.1175/JCLI-D-14-00582.1 493 494 MacLachlan C, Arribas A, Peterson KA, et al (2015) Global Seasonal forecast system version 5 (GloSea5): A high-resolution seasonal forecast system. Q J R Meteorol Soc 141:1072– 495 1084. https://doi.org/10.1002/qj.2396 496 Marshall AG, Hudson D, Wheeler MC, et al (2014) Intra-seasonal drivers of extreme heat 497 over Australia in observations and POAMA-2. Clim Dyn 43:1915–1937. 498 https://doi.org/10.1007/s00382-013-2016-1 499 500 McIntosh PC, Hendon HH (2017) Understanding Rossby wave trains forced by the Indian 501 Ocean Dipole. Clim Dyn 0:1–16. https://doi.org/10.1007/s00382-017-3771-1 Rao J, Garfinkel CI, White IP, Schwartz C (2020) The Southern Hemisphere Sudden 502 503 Stratospheric Warming in September 2019 and its predictions in S2S Models. Submitted to JGR. 504 Rayner, N.A.A., Parker, D.E., Horton, E.B., Folland, C.K., Alexander, L.V., Rowell, D.P., 505 Kent, E.C. and Kaplan, A. (2003) Global analyses of sea surface temperature, sea ice, 506 and night marine air temperature since the late nineteenth century. Journal of 507 Geophysical Research: Atmospheres, 108 (D14). 508 Reynolds RW, Rayner NA, Smith TM, et al (2002) An improved in situ and satellite SST 509 analysis for climate. J Clim 15:1609-1625. https://doi.org/10.1175/1520-510 0442(2002)015<1609:AIISAS>2.0.CO;2 511 Risbey JS, Monselesan DP, O'Kane TJ, et al (2019) Synoptic and Large-Scale Determinants 512 of Extreme Austral Frost Events. J Appl Meteorol Climatol 58:1103–1124. 513

514	https://doi.org/10.1175/JAMC-D-18-0141.1		
515	Risbey JS, Pook MJ, McIntosh PC, et al (2009) On the Remote Drivers of Rainfall		
516	Variability in Australia. Mon Weather Rev 137:3233–3253.		
517	https://doi.org/10.1175/2009MWR2861.1		
518	Saji NH, Ambrizzi T, Ferraz SET (2005) Indian Ocean Dipole mode events and austral		
519	9 surface air temperature anomalies. Dyn Atmos Ocean 39:87–101.		
520	0 https://doi.org/10.1016/j.dynatmoce.2004.10.015		
521	Saji NH, Goswami BN, Vinayachandran PN, Yamagata T (1999a) A dipole mode in the		
522	tropical Indian Ocean. Nature 401:360-363. https://doi.org/10.1038/43854		
523	Saji NH, Goswami BN, Vinayachandran PN, Yamagata T (1999b) A dipole mode in the		
524	tropical Indian Ocean. Nature 401:360–363. https://doi.org/10.1038/43854		
525	Shi L, Hendon HH, Alves O, et al (2012) How Predictable is the Indian Ocean Dipole? Mon		
526	Weather Rev 140:3867–3884. https://doi.org/10.1175/MWR-D-12-00001.1		
527	Thompson DWJ, Wallace JM (2000) Annular Mode in the extratropical circulation. Part I:		
528	Month-to-month variability. J Clim 13:1000–1016.		
529	https://doi.org/http://dx.doi.org/10.1175/1520-		
530	0442(2000)013<1000:AMITEC>2.0.CO;2		
531	Ummenhofer CC, England MH, McIntosh PC, et al (2009) What causes southeast Australia's		
532	worst droughts? Geophys Res Lett 36:L04706. https://doi.org/10.1029/2008GL036801		
533	Wang G, Hendon HH (2007) Sensitivity of Australian Rainfall to Inter-El Niño Variations. J		
534	Clim 20:4211–4226. https://doi.org/10.1175/JCLI4228.1		
535	Webster JR, Stewart M, Rogers AR, Verkerk GA (2008) Assessment of welfare from		
536	physiological and behavioural responses of New Zealand dairy cows exposed to cold		

537	and wet conditions. Animal Welfare. Anim Welf 17:19-26		
538	Wilks DS (2006) Statistical methods in the atmospheric sciences, Second Edi. Academic		
539	Press, Inc.		
540	Zhang X, Alexander L, Hegerl GC, et al (2011) Indices for monitoring changes in extremes		
541	based on daily temperature and precipitation data. WIREs Clim Chang 2:851-870		
542	Zhao M, Hendon HH (2009) Representation and prediction of the Indian Ocean Dipole in the		
543	POAMA seasonal forecast model. Q J R Meteorol Soc 135:337–352.		
544	https://doi.org/10.1002/qj.370		
545	Zheng B, Chapman SC, Christopher JT, et al (2015) Frost trends and their estimated impact		
546	on yield in the Australian wheatbelt. 66:3611–3623. https://doi.org/10.1093/jxb/erv163		
547			
548	Figure captions		
549	Figure 1. Deciles of monthly mean of daily minimum temperatures for (a) August and (b)		
550	September 2019. Deciles are computed based on 1910-2019.		
551	(http://www.bom.gov.au/jsp/awap/temp/index.jsp).		
552	Figure 2. September 2019 anomalies of (a) Tmin, (b) lowest Tmin, (c) number of days when		
553			
	Tmin is below 0 °C and (d) number of days when Tmin is below 2 °C compared to their		
554	Tmin is below 0 °C and (d) number of days when Tmin is below 2 °C compared to their respective climatologies over the period 1990-2012. Note that in (c) and (d) the increased		
554555	·		
	respective climatologies over the period 1990-2012. Note that in (c) and (d) the increased		
555	respective climatologies over the period 1990-2012. Note that in (c) and (d) the increased number of days with night-time temperatures below 0 and 2 °C is shown with the blue colour		
555 556	respective climatologies over the period 1990-2012. Note that in (c) and (d) the increased number of days with night-time temperatures below 0 and 2 °C is shown with the blue colour shading.		

correlation in panel (a), displaying lower monthly Tmin positively correlated with lower lowest Tmin whereas red shading indicates positive correlation and blue shading indicates negative correlation in (b) and (c), displaying monthly Tmin negatively correlated with the number of extreme cold nights (i.e. lower monthly Tmin is associated with increased number of days with Tmin < 0 °C and < 2 °C in (b) and (c), respectively). Spearman rank correlation is used because the extreme threshold-based indices are non-Gaussian and therefore require analysis using non-parametric methods.

Figure 4. (a) De-trended SST anomalies for September 2019, (b) regression of SST on the inversely signed eastern Australian Tmin averaged over land points of 140-156°E, 45-10°S for September 1979-2018, and (c) time series of the Indian Ocean Dipole mode index (DMI; dark blue bars), the El Nino Modoki Index (EMI; orange bars), and the areal-mean eastern Australian Tmin of September (EAU Tmin; light blue bars). In (b) regression coefficients are scaled by the magnitude of EAU Tmin in 2019. Stippling in (b) indicates the statistical significance of the regression coefficients at the 10% level.

Figure 5. Spearman's rank correlation of (a,b) September-mean Tmin, (c,d) number of days in September with Tmin < 0 °C, (e,f) number of days in September with Tmin < 2 °C, and (g,h) lowest Tmin during September with the DMI (left) and the EMI (right). Positive correlation is shown with blue colour shading in (c)-(f) to indicate positive DMI and EMI are associated with increased days for Tmin < 0 °C and < 2 °C.

Figure 6. (a) Pearson correlation between the observed Tmin and the reconstruction of Tmin using the DMI and the EMI over 1979-2018, (b) observed Tmin anomalies for September 2019 (same as Fig 2a), and (c) reconstruction of Tmin anomalies for September 2019 using the same the multiple linear regression model as in (a). The pattern correlation between (b) and (c) is 0.8.

Figure 7. (Top row; a-e) September 2019 anomalies of (a) MSLP (hPa), (b) 10-m zonal wind (ms⁻¹), (c) 10-m meridional wind (ms⁻¹), (d) total cloud cover fraction (%), and (e) Tmin (°C). (Middle row; f-j) Respective composites of the same fields as in (a)-(e) for the five strongest positive IOD years in 1979-2018 (listed in Table 1). (Bottom row; k-o) Same as (f-j) but for the three strongest central Pacific El Nino years (listed in Table 1). Anomalies of total cloud cover fraction were computed relative to the climatological fraction. Colour bars for the middle and bottom row are at the bottom. Note that for (d), (i), (n) red colour shading indicates the reduction of the cloud cover and blue colour shading indicates the increase of the cloud cover. Stippling in the middle and bottom rows indicates the statistical significance on the difference of the two means (composite mean vs climatological mean) at the 10% level, assessed by the two-tailed Student t-test with the samples sizes of five and three in the composite groups of the strong positive IOD and the strong central Pacific El Nino, respectively, and 23 in the climatological group. Figure 8. (a) ACCESS-S1 hindcast skill to predict the DMI as a function of forecast start month (y-axis) and lead time (x-axis). (b) Same as (a) except for the EMI. (c) Forecasts for DMI and EMI September 2019 from different start times (orange colour bars). The red colour bars in (c) are the observed amplitudes of the DMI and the EMI. Figure 9. (a,b) Forecast ROC displayed as a function of hit rates versus false alarm rates using all the land points over Australia in the hindcast period 1990-2012 at lead times of 0 and 1 month, respectively. The blue dots indicate the probability thresholds to define the positive forecast for an event. The diagonal line indicates no skill. (c,d) Forecast skill measured by the area under the ROC curve for predicting bottom quintile Tmin for

584

585

586

587

588

589

590

591

592

593

594

595

596

597

598

599

600

601

602

603

604

605

606

607

Figure 10. Forecasts from ACCESS-S1 for (a,b) Tmin (°C), (c,d) outgoing longwave

September at lead time 0 and 1 month at each grid point.

radiation flux (Wm⁻²), (e,f) MSLP, and (g,h) 500 hPa geopotential height (m) anomalies for 608 September 2019 at 0 and 1 month lead times. 609 Figure 11. Composites of ensemble mean forecast anomalies at lead time zero for (a,f) 610 611 MSLP (hPa), (b,g) 10-m zonal wind (ms⁻¹), (c,h) 10-m meridional wind (ms⁻¹), (d,i) outgoing longwave radiation flux, (Wm⁻²), and (e,j) Tmin (°C) during the three strongest positive IOD 612 years (upper panels) and the three strongest central Pacific El Nino years (lower panels). The 613 years for each category are listed in Table 1. Stippling indicates the statistical significance on 614 the difference of the two means at the 10% level, assessed by a Student t-test with the sample 615 sizes of three in the composite groups and 23 in the climatological group. 616

617

	Positive (> 1σ)	Negative (< -1σ)
DMI	1994 1997 2006 2015 2018	1992 1998 2005 2010 2016
EMI	1994 2002 2004	1983 1988 1998 2008 2010 2016

Table 1. The strongest positive and negative IOD and central Pacific El Nino years based on
 September-mean absolute values of the DMI and the EMI being at least greater than 1
 standard deviation for 1990-2012.

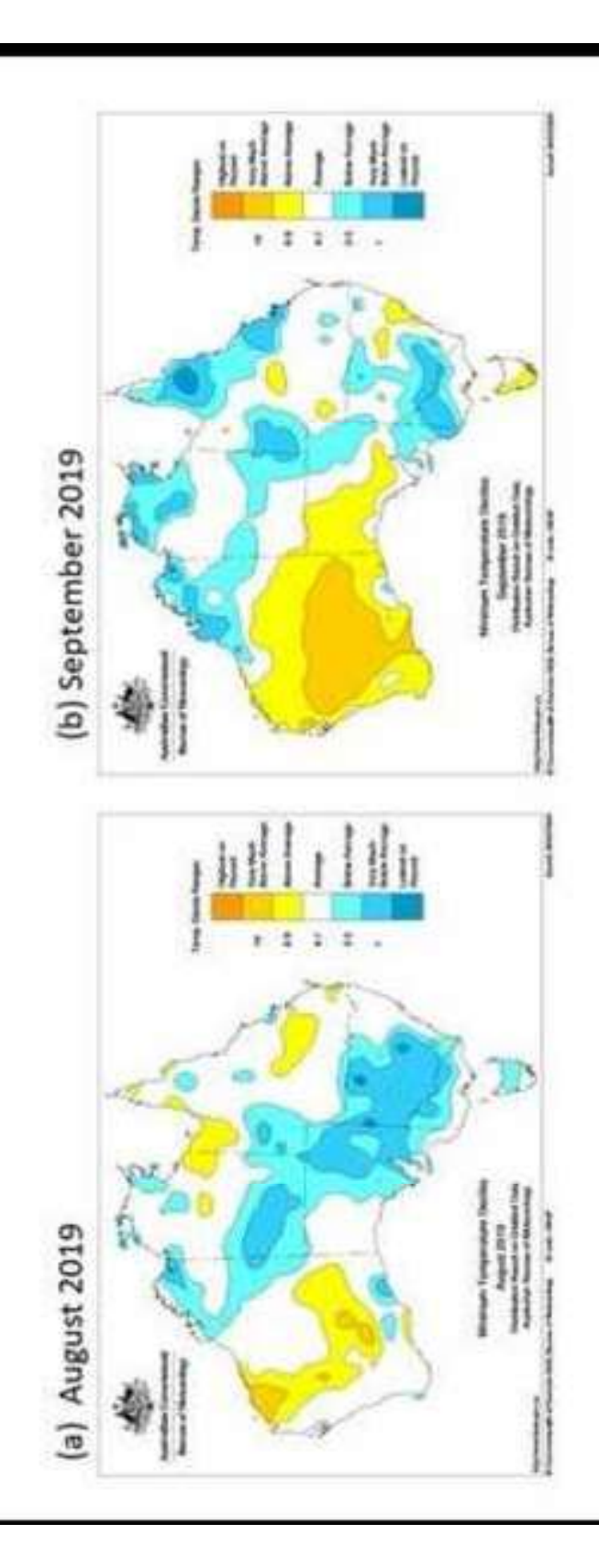
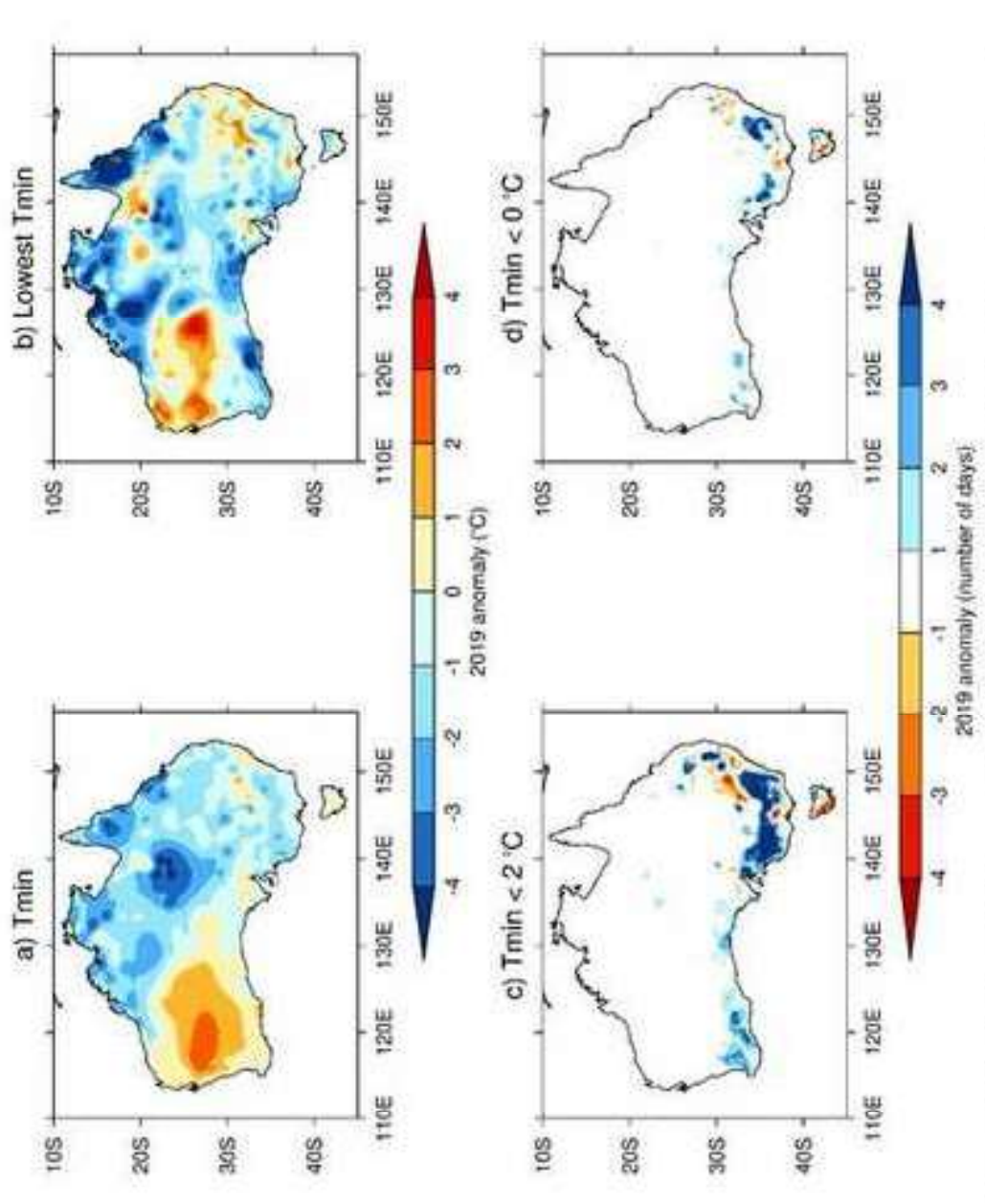


Figure 1. Deciles of monthly mean of daily minimum temperatures for (a) August and (b) September 2019. Deciles are computed based on 1910-2019. Data are from http://www.bom.gov.au/isp/awap/temp/index.jsp



number of days with night-time temperatures below 0 and 2 °C is shown with the blue colour Figure 2. September 2019 anomalies of (a) Imin, (b) lowest Imin, (c) number of days when respective climatologies over the period 1990-2012. Note that in (c) and (d) the increased Tmin is below 0 °C and (d) number of days when Tmin is below 2 °C compared to their shading

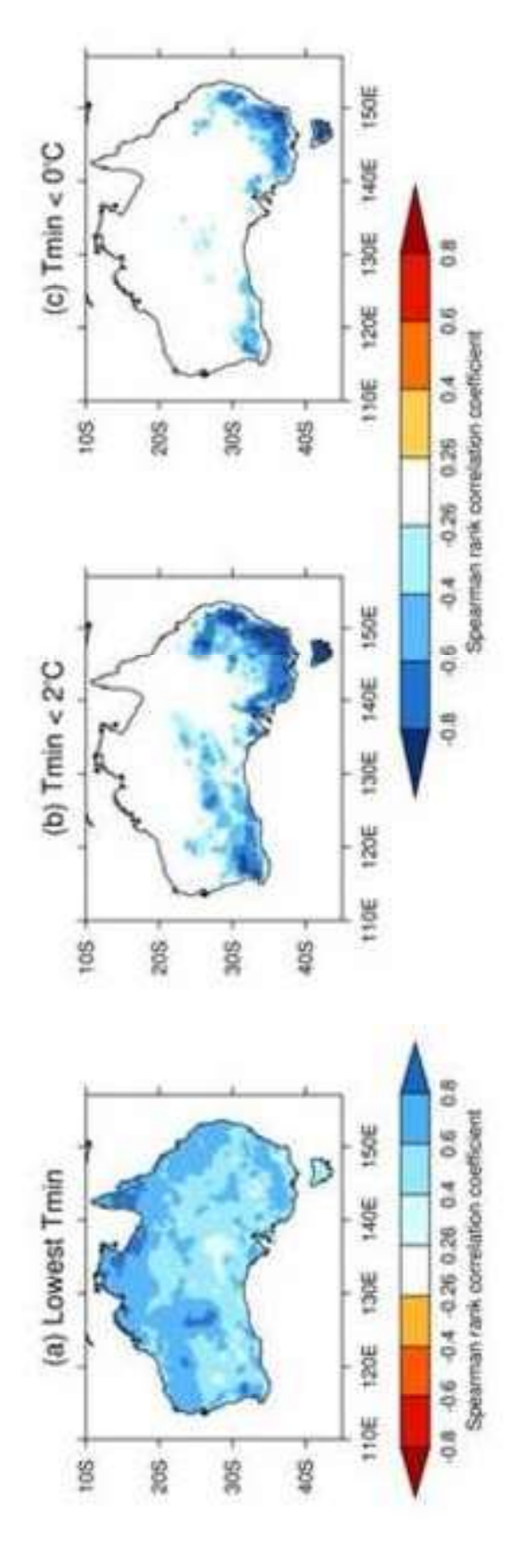


Figure 3. Spearman rank correlation of monthly Tmin with (a) lowest Tmin, (b) number of days (c), displaying monthly Tmin negatively correlated with the number of extreme cold nights (i.e. when Tmin is below 0 °C and (c) number of days when Tmin is below 2 °C in September. Note shading indicates positive correlation and blue shading indicates negative correlation in (b) and lower monthly Tmin is associated with increased number of days with Tmin < 0 °C and < 2 °C (a), displaying lower monthly Tmin positively correlated with lower lowest Tmin whereas red in (b) and (c), respectively). Spearman rank correlation is used because the extreme thresholdthat red shading indicates negative correlation and blue indicates positive correlation in panel based indices are non-Gaussian and therefore require analysis using non-parametric methods

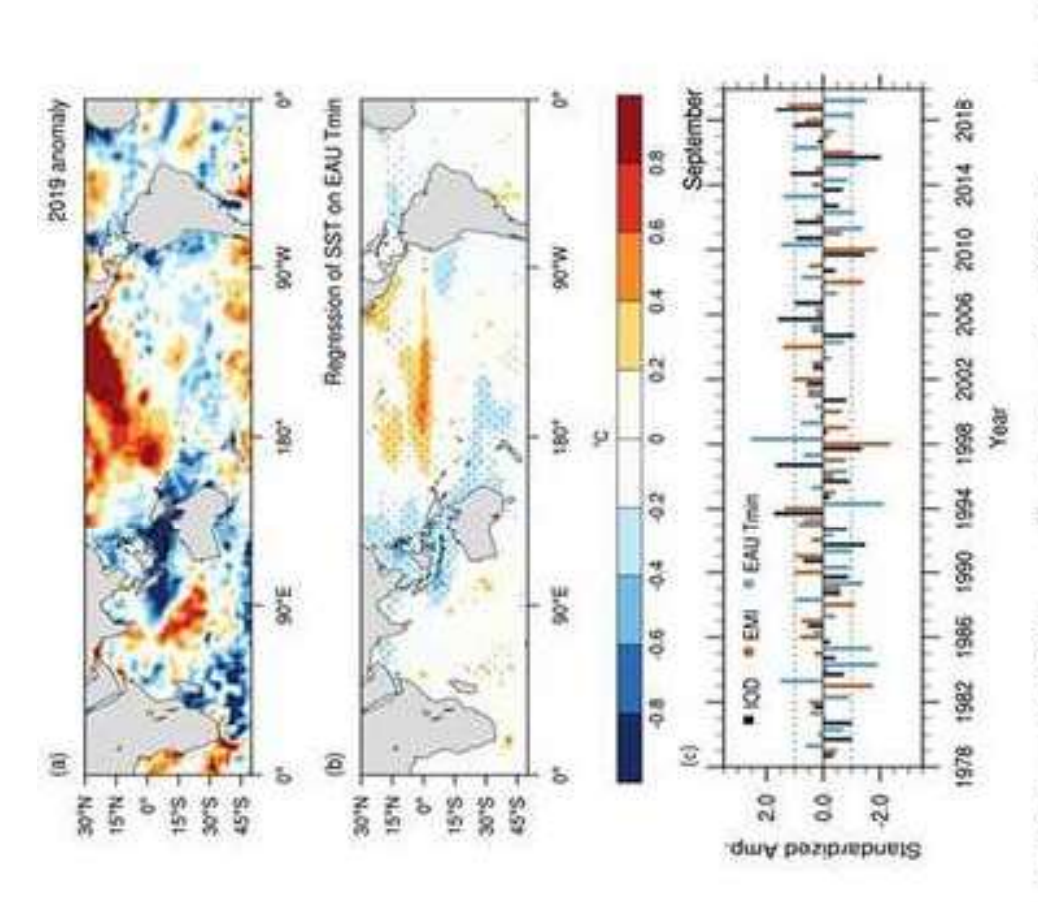
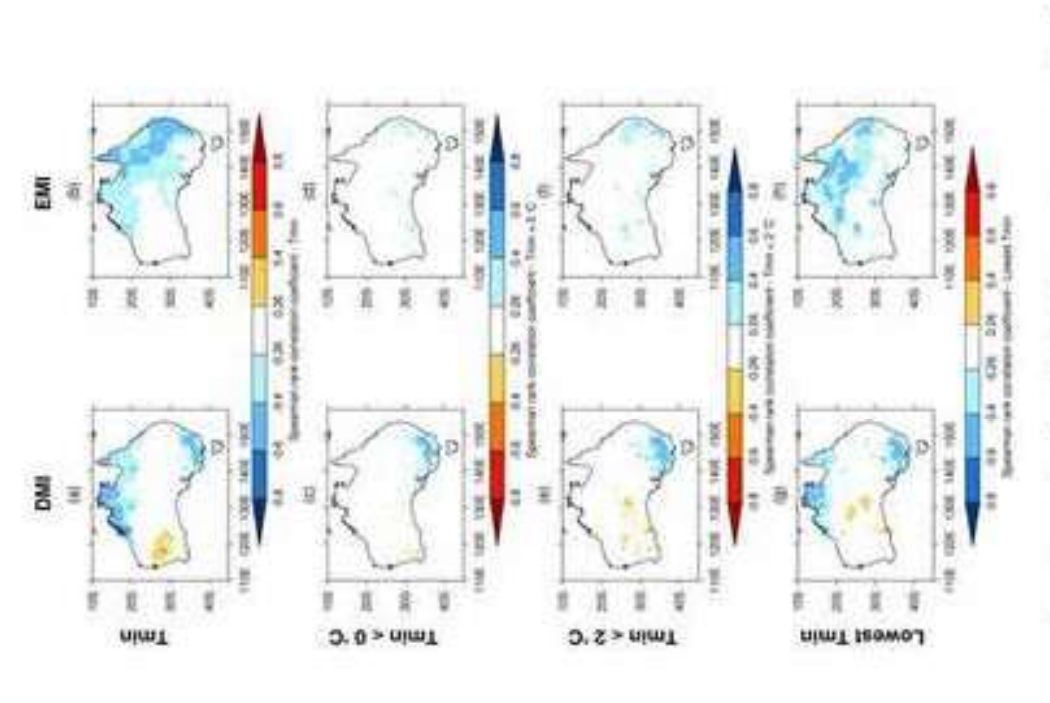
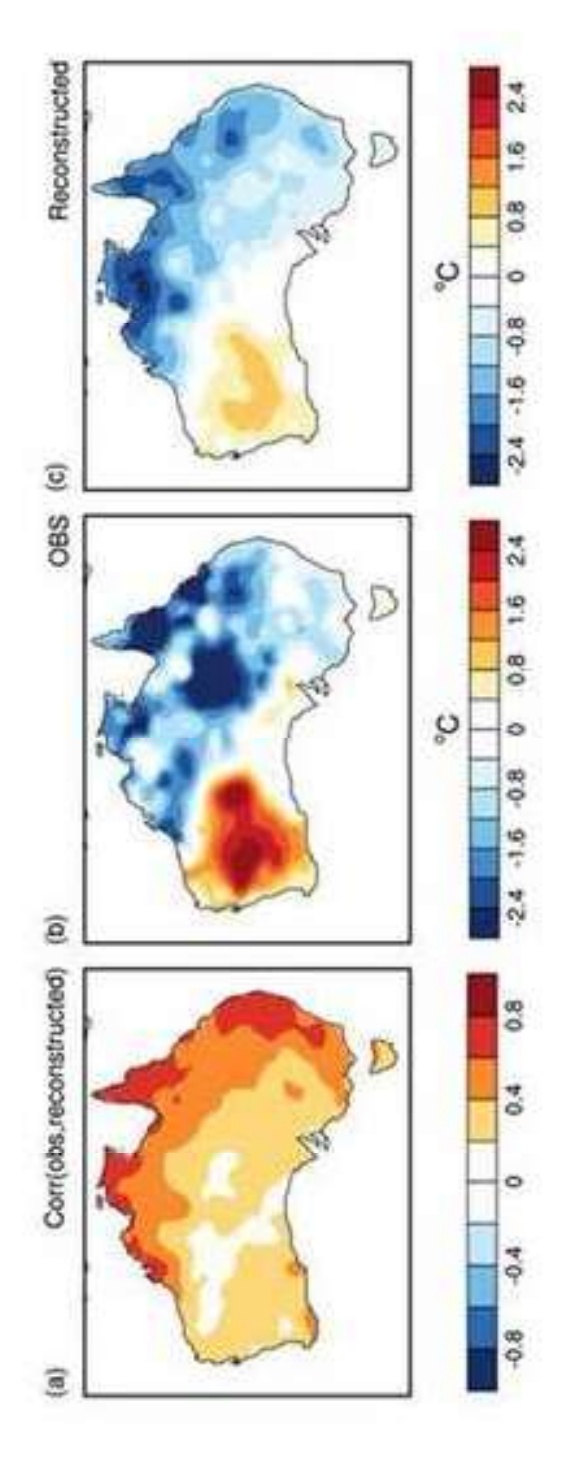


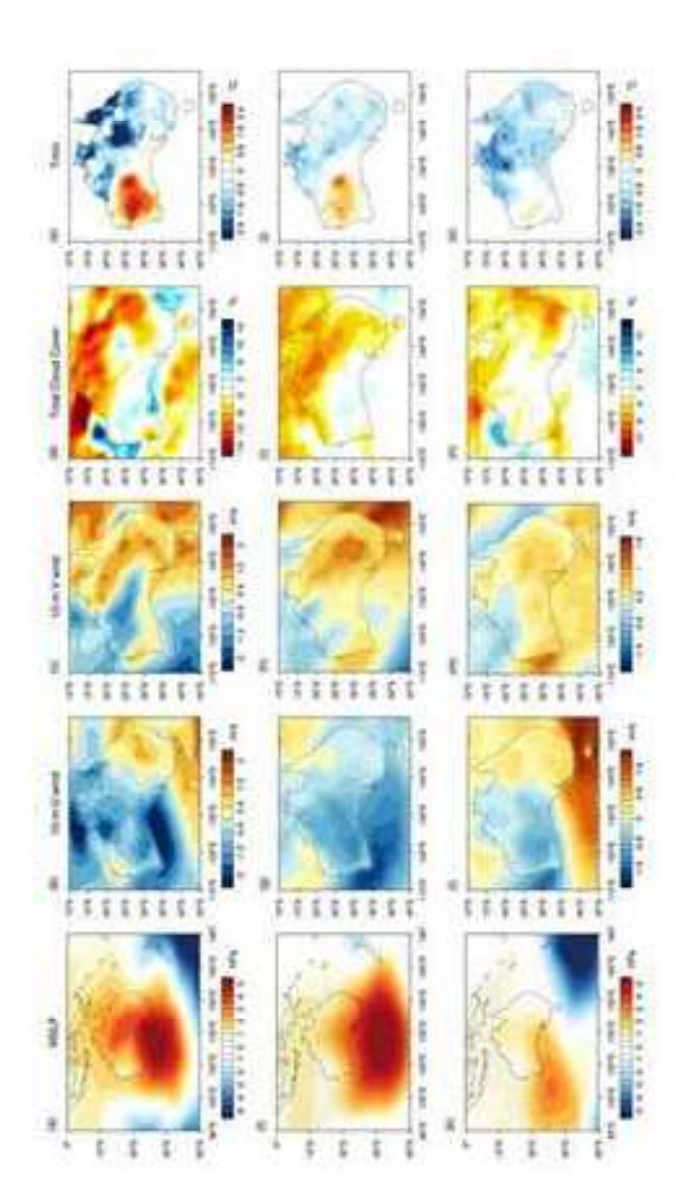
Figure 4. (a) De-trended SST anomalies for September 2019, (b) regression of SST on the inversely signed eastern Australian Tmin September (EAU Tmin; light blue bars). In (b) regression coefficients are scaled by the magnitude of EAU Tmin in 2019. Stippling averaged over land points of 140-156°E, 45-10°S for September 1979-2018, and (c) time series of the Indian Ocean Dipole mode index (DMI; dark blue bars), the El Nino Modoki Index (EMI; orange bars), and the areal-mean eastern Australian Tmin of in (b) indicates the statistical significance of the regression coefficients at the 10% level.



shown with blue colour shading in (c)-(f) to indicate positive DMI and EMI are associated with Figure 5. Spearman's rank correlation of (a,b) September-mean Tmin, (c,d) number of days in lowest Tmin during September with the DMI (left) and the EMI (right). Positive correlation is September with Tmin < 0 °C, (e,f) number of days in September with Tmin < 2 °C, and (g,h) increased days for Tmin < 0 °C and < 2 °C.



the multiple linear regression model as in (a). The pattern correlation between (b) and (c) is 0.8. using the DMI and the EMI over 1979-2018, (b) observed Tmin anomalies for September 2019 (same as Fig 2a), and (c) reconstruction of Tmin anomalies for September 2019 using the same Figure 6. (a) Pearson correlation between the observed Imin and the reconstruction of Imin



(composite mean vs climatological mean) at the 10% level, assessed by the two-tailed. Student t-test with the samples sizes of five and three in the cloud cover fraction (%), and (e) Train (°C). (Middle row, f-j) Respective composites of the same fields as in (a)-(e) for the five strongest positive row are at the bottom. Note that for (d), (i), (n) red colour shading indicates the reduction of the cloud cover and blue colour shading indicates the Figure 7. (Top row, a-e) September 2019 anomalies of (a) MSLP (hPa), (b) 10-m zonal wind (ms-1), (c) 10-m meridional wind (ms-1), (d) total Table 1). Anomalies of total cloud cover fraction were computed relative to the canatological fraction. Colour bars for the middle and bottom increase of the cloud cover. Suppling in the middle and bottom rows indicates the statistical significance on the difference of the two means 10D years in 1979-2018 (listed in Table 1). (Bottom row; k-o) Same as (f-j) but for the three strongest central Pacific El Nino years (listed composite groups of the strong positive IOD and the strong central Pacific El Nino, respectively, and 23 in the climatological group

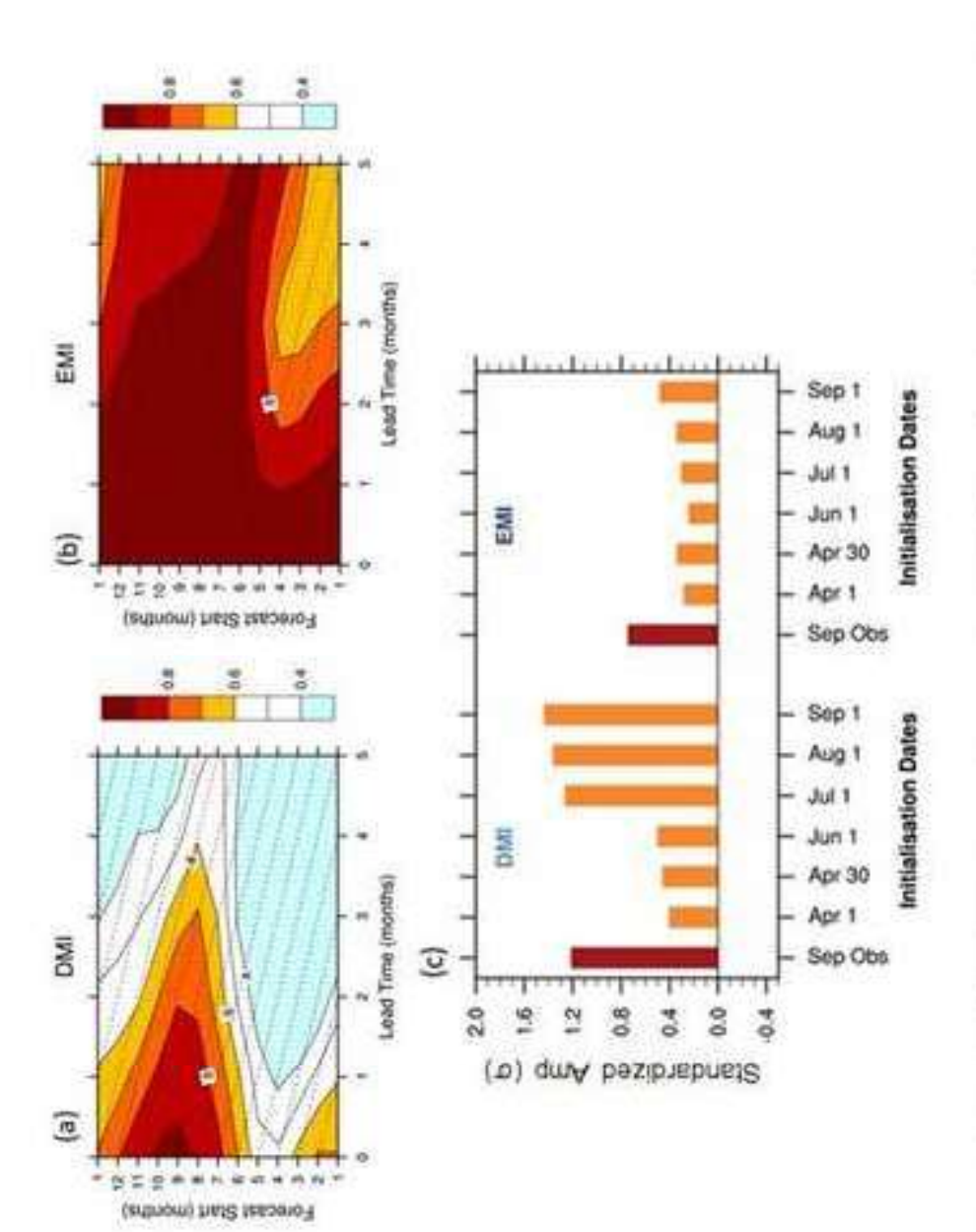
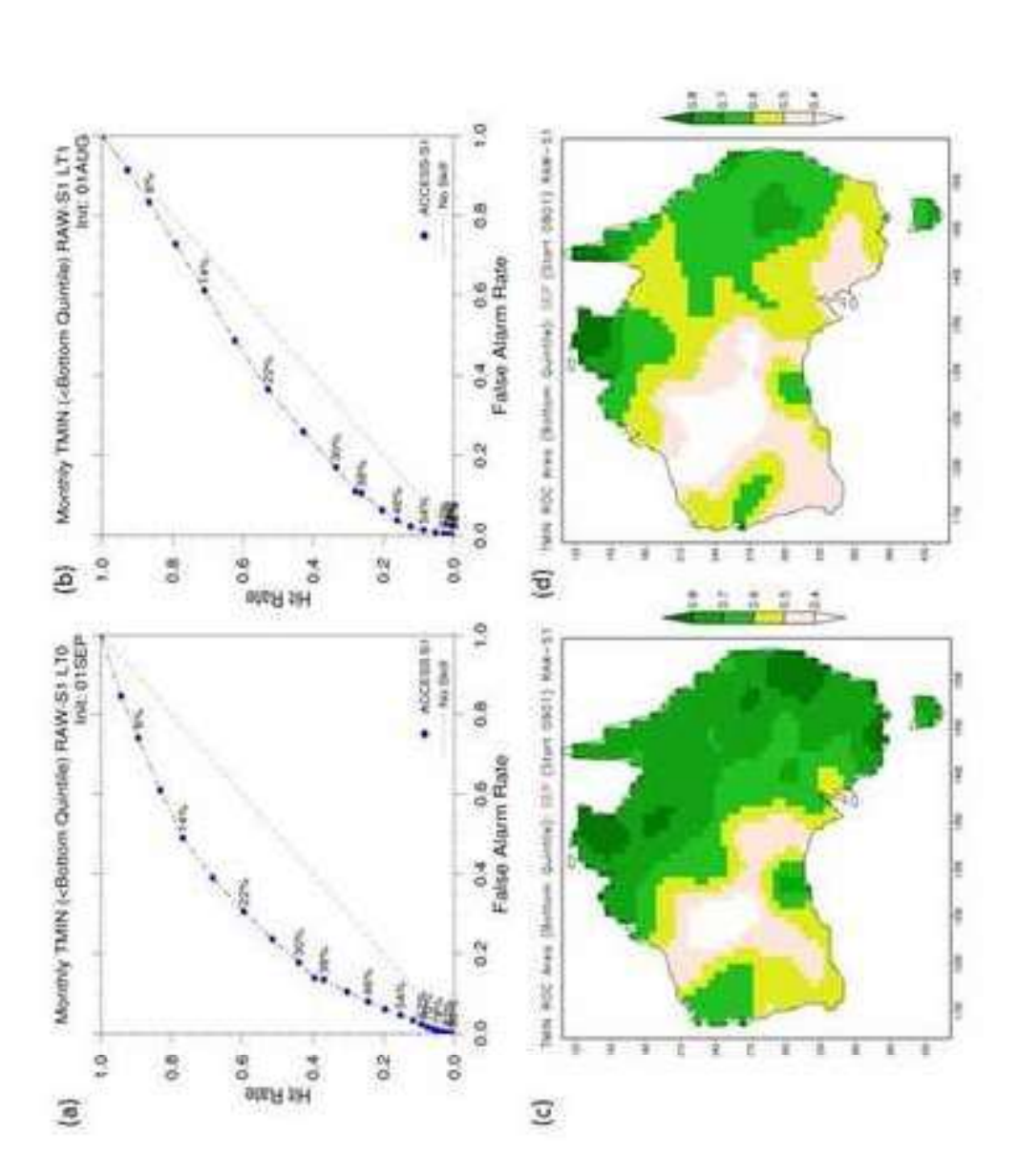


Figure 8. (a) ACCESS-SI hindcast skill to predict the DMI as a function of forecast start month EMI September 2019 from different start times (orange colour bars). The red colour bars in (c) (y-axis) and lead time (x-axis). (b) Same as (a) except for the EMI. (c) Forecasts for DMI and are the observed amplitudes of the DMI and the EMI.



area under the ROC curve for predicting bottom quintile Tmin for September at lead time 0 and Figure 9. (a,b) Forecast ROC displayed as a function of hit rates versus false alarm rates using forecast for an event. The diagonal line indicates no skill. (c,d) Forecast skill measured by the month, respectively. The blue dots indicate the probability thresholds to define the positive all the land points over Australia in the hindcast period 1990-2012 at lead times of 0 and 1 I month at each grid point

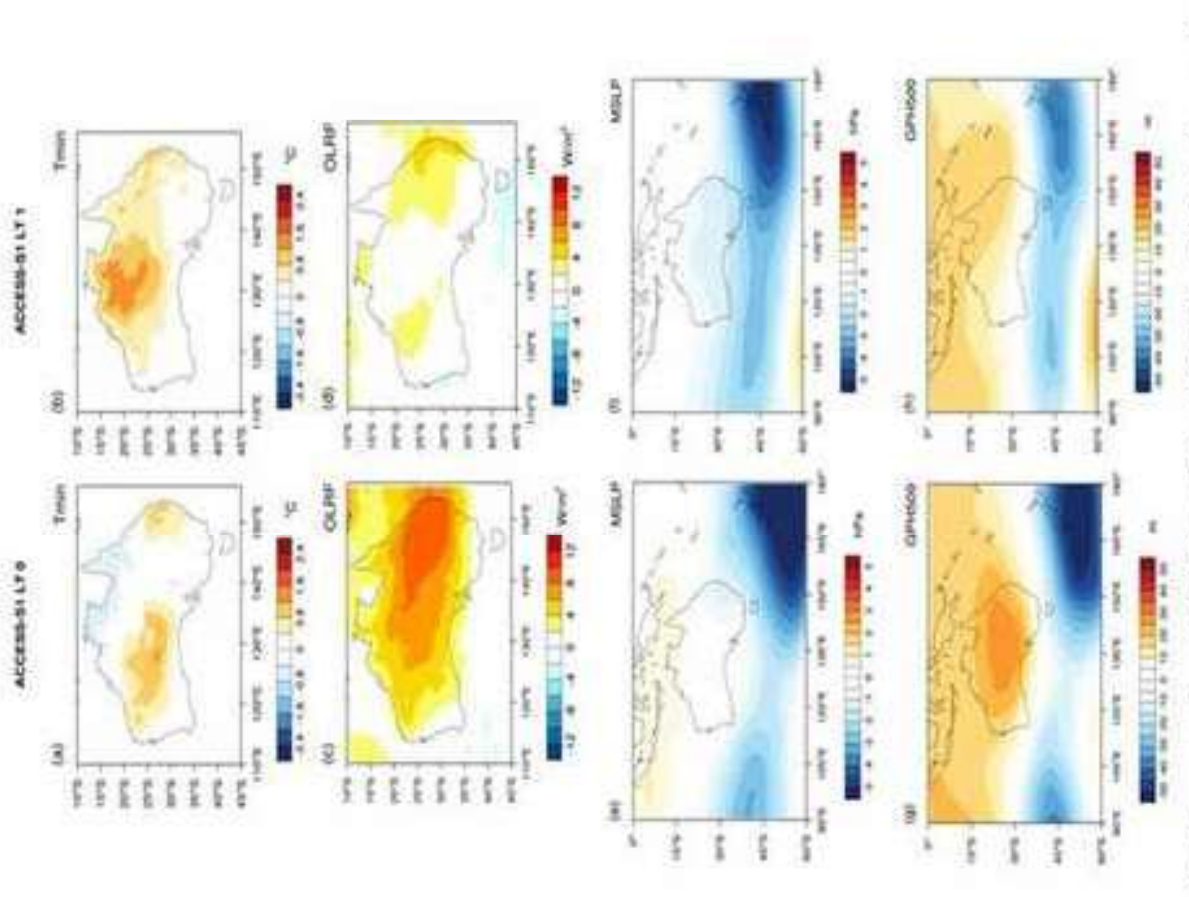
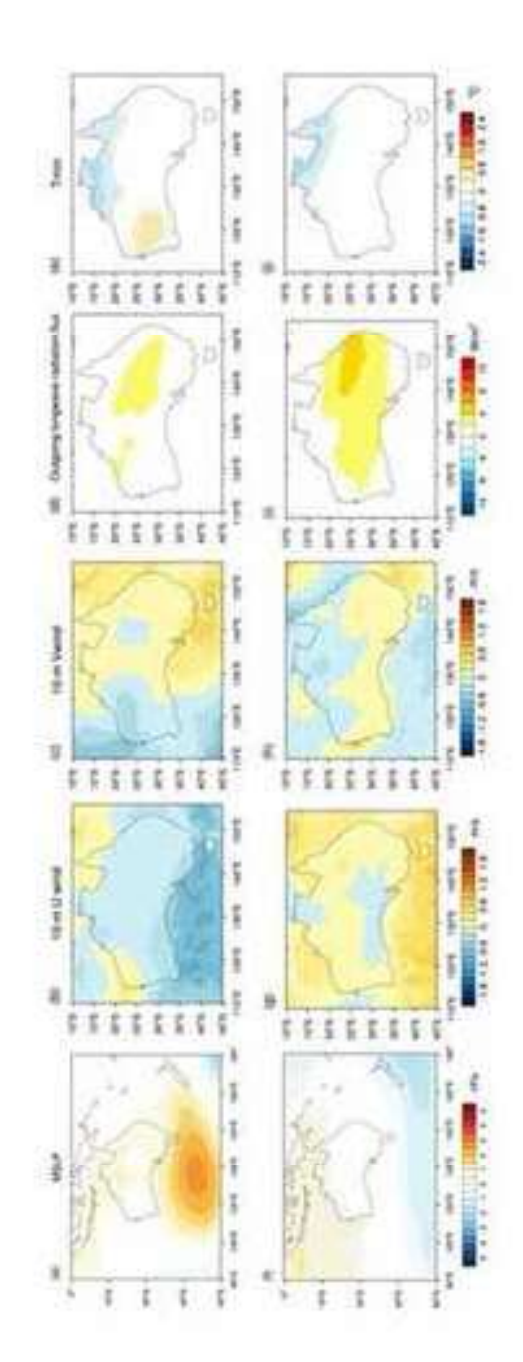


Figure 10. Forecasts from ACCESS-S1 for (a,b) Tmin (°C), (c,d) outgoing longwave radiation flux (Wm⁻²), (e,f) MSLP, and (g,h) 500 hPa geopotential height (m) anomalies for September 2019 at 0 and 1 month lead times



MSLP (hPa), (b,g) 10-m zonal wind (ms-1, (c,h) 10-m meridional wind (ms-1), (d,i) outgoing years (upper panels) and the three strongest central Pacific El Nino years (lower panels). The years for each category are listed in Table 1. Stippling indicates the statistical significance on the difference of the two means at the 10% level, assessed by a Student t-test with the sample longwave radiation flux, (Wm-3), and (e.j) Tmin (°C) during the three strongest positive IOD Figure 11. Composites of ensemble mean forecast anomalies at lead time zero for (a,f) sizes of three in the composite groups and 23 in the climatological group.

Supplementary Material for:

Tropical forcing of Australian extreme low minimum temperatures in September 2019

Eun-Pa Lim¹, Harry H. Hendon¹, Li Shi¹, Catherine de Burgh-Day¹, Debra Hudson¹, Andrew King², Blair Trewin¹, Morwenna Griffiths¹ and Andrew Marshall¹

Corresponding to harry.hendon@bom.gov.au

To be submitted to Climate Dynamics

Contents: Figures S1-S7

¹ Bureau of Meteorology, Melbourne, VIC, Australia

² School of Earth Sciences and ARC Centre of Excellence for Climate Extremes, University of Melbourne, Parkville, VIC, Australia

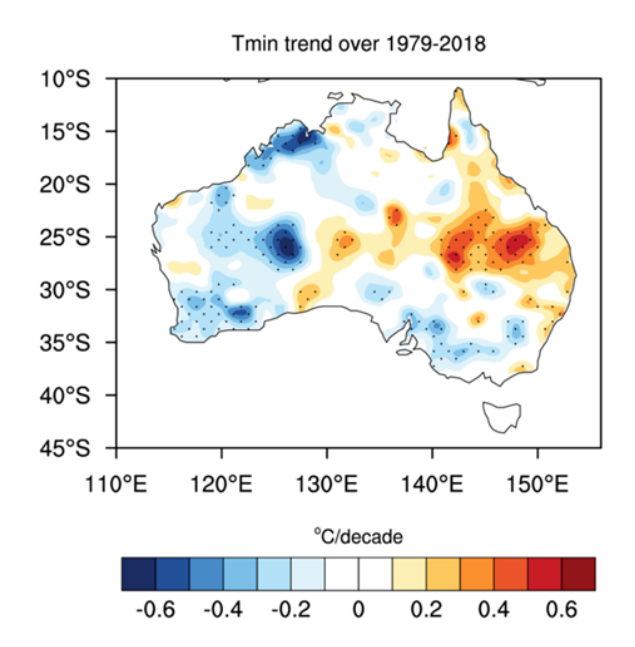
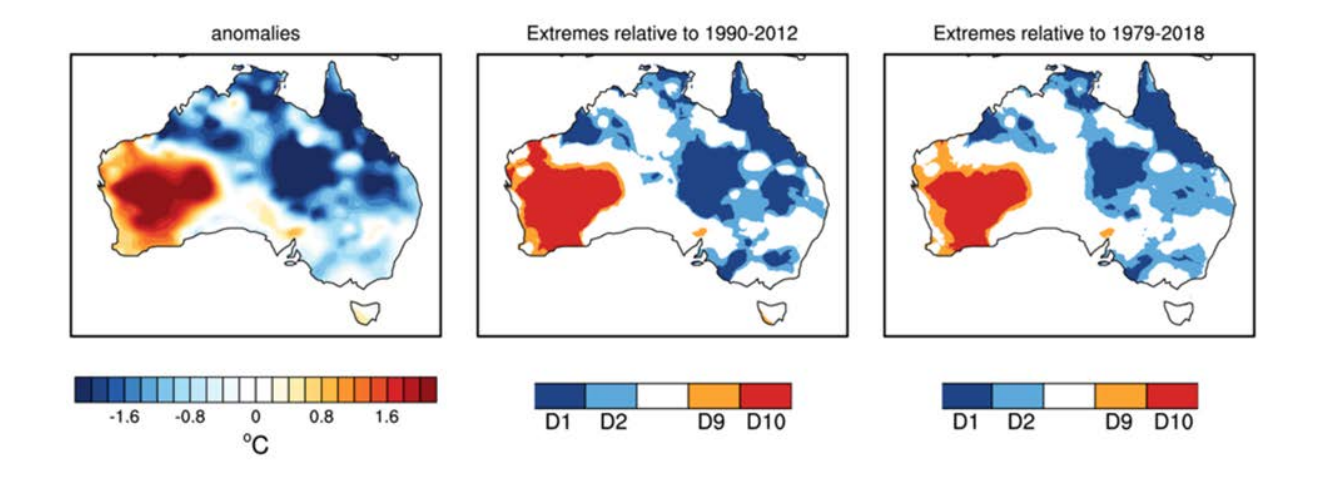


Figure S1. Linear trend on September Tmin over 1979-2018 (°C per decade). Stippling indicates statistically significant trends at the 10% level assessed by a two-tailed Student t-test with 39 degrees of freedom.



Figures S2. (a) Tmin anomalies of September 2019 and (b,c) its decile maps with the decile thresholds found in 1990-2012 (when ACCESS-S1 hindcasts are available) and 1979-2018

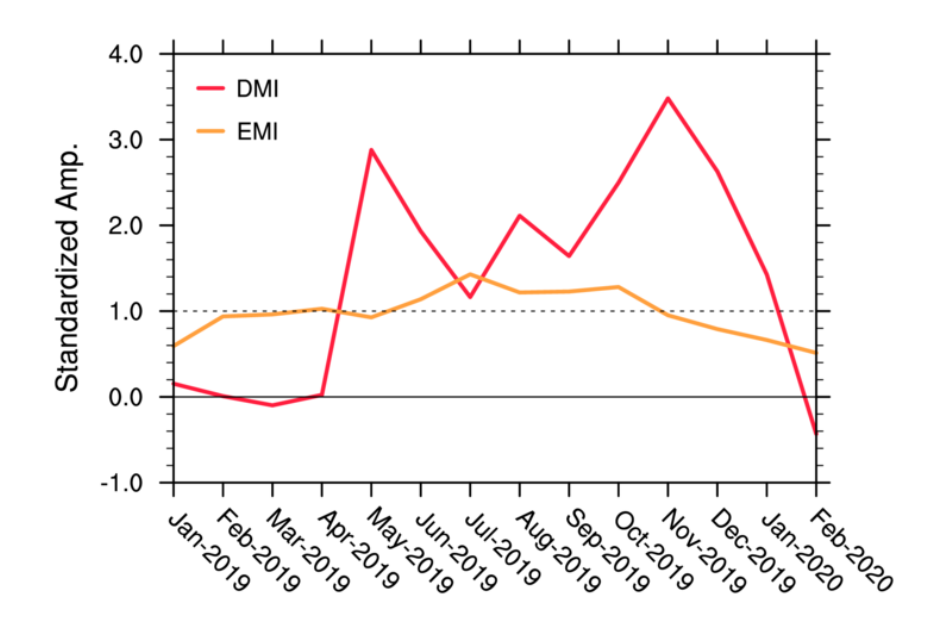


Figure S3. Standardized anomalies of the IOD mode index (DMI) and the El Nino Modoki Index (EMI) in January 2019 to February 2020, which were computed relative to the monthly climatology and standard deviations of 1990-2012.

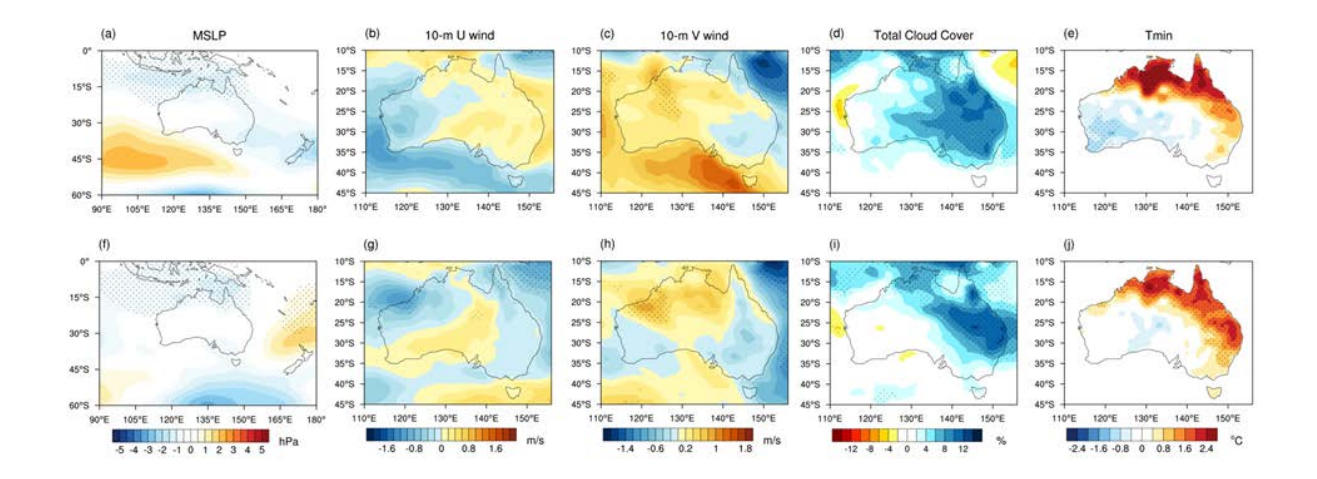


Figure S4. (Top row; a-e) Composites of (a) MSLP (hPa), (b) 10-m zonal wind (ms⁻¹), (c) 10-m meridional wind (ms⁻¹), (d) total cloud cover fraction (%), and (e) Tmin (°C) anomalies for the five strongest negative IOD years in 1979-2018 as listed in Table 1; (Bottom row f-j) Same as (a-e) but for the six strongest central Pacific La Nina years. Stippling indicates the statistical significance on the difference of the two means at the 10% level, assessed by a two-tailed Student t-test with five and six samples in the negative IOD and the central Pacific La Nina composite groups, respectively, and 23 samples in the climatological group. Note that strong negative IOD and strong central Pacific La Nina occurred in 1998 and 2010, so these two years are included both composites, which may partly explain the similarities between the two composites.

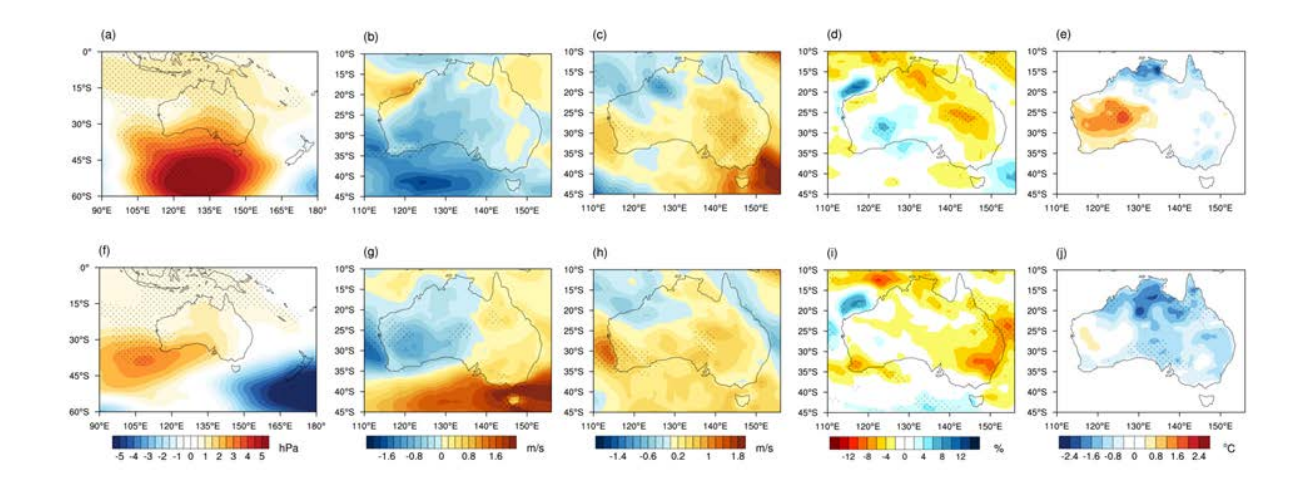


Figure S5. (Top row; a-e) Composites of September (a) MSLP (hPa), (b) 10-m zonal wind (ms⁻¹), (c) 10-m meridional wind (ms⁻¹), (d) total cloud cover fraction (%) and (e) Tmin (°C). anomalies for the three strongest positive IOD years in 1990-2012 (listed in Table 1) for the direct comparison with the forecast composites shown in Figure 11 in the main article. (Bottom row; f-j) Same as (a-e) but for the three strongest central Pacific El Nino years (listed in Table 1). Stippling indicates the statistical significance on the difference of the two means (composite mean vs climatological mean) at the 10% level, assessed by the two-tailed Student t-test with the samples sizes of five and three in the composite groups of the strong positive IOD and the strong central Pacific El Nino, respectively, and 23 in the climatological group.

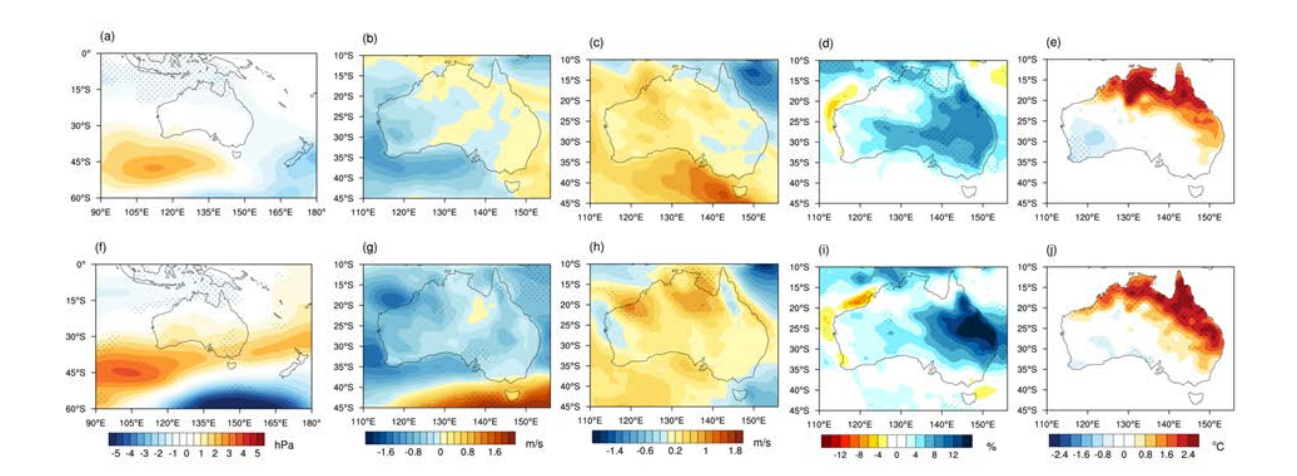


Figure S6. The same as Figure S4 except four negative IOD years and three central Pacific La Nina years being used for the direct comparison with the forecast composites in Figure S7.

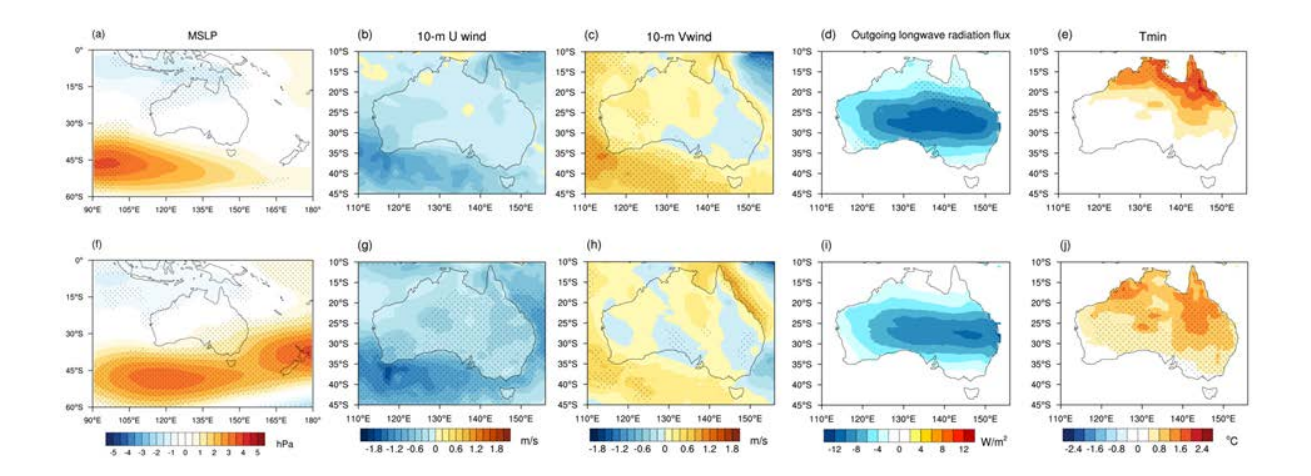


Figure S7. Ensemble mean forecast composites of (a,f) MSLP, (b,g) 10-m zonal wind (ms⁻¹), (c,h) 10-m meridional wind (ms⁻¹), (d,i) total cloud cover fraction (%), and (e,j) Tmin (°C) during the four strong negative IOD years (upper panels) and the three strong central Pacific La Nina years (lower panels) at lead time 0 as found in Table 1 and in the hindcast period of 1990-2012. Stippling indicates the statistical significance computed as described in Figure S4 caption except four and three samples in the negative IOD and the central Pacific La Nina composite groups, respectively, being used.